Met. Mater. Int., Vol. 18, No. 6 (2012), pp. 957~964
doi: 10.1007/s12540-012-6007-2

Microstructural, Tribological and Electrochemical Corrosion Studies on Reactive DC Magnetron Sputtered Zirconium Nitride Films with Zr Interlayer on Steel

B. Subramanian[1,*], V. Swaminathan[2], and M. Jayachandran[1]

[1]Electrochemical Materials Science Division, CSIR-Central Electrochemical Research Institute, Karaikudi 630-006, India
[2]Nanyang Technological University 639-798, Singapore

(received date: 20 October 2011 / accepted date: 3 January 2012)

Thin films of Zirconium Nitride (ZrN) were deposited by DC magnetron sputtering. The structure of the films was examined by X-ray diffraction and the crystallographic parameters were refined by Rietveld analysis. The columnar micro-structure was observed via cross-sectional SEM analysis. Defect induced, first order spectra were observed from Laser Raman studies. XPS showed the presence of Zr (N,O) ZrO_2 phases on the surface of the film. The pitting corrosion was substantially reduced by the employment of Zr film as an interlayer. Corrosion tests revealed that ZrN films with a Zr interlayer exhibited clear passivation characteristics with considerably better corrosion resistance than the film without an interlayer.

Key words: thin films, sputtering, corrosion, crystal structure, X-ray diffraction

1. INTRODUCTION

Zirconium nitride (ZrN), a compound of the period V, exhibits suitable properties for a great variety of industrial applications. It has been attracting attention for its superior mechanical properties and corrosion resistance [1,2]. Stoichiometric ZrN compound is the only stable phase with a gold-like colour due to its metallic band structure. Other non-stoichiometric metastable phases also exist such as Zr_2N, $Zr\ N_2$, Zr_3N_4 and Zr_4N_3 [3]. The ZrN_y thin films crystallize in to a FCC NaCl structure type over a large chemical composition range ($0.7<y<1.2$). They exhibit a columnar morphology with preferential (111) crystallite orientation [4]. The structure and properties of ZrN films prepared by reactive triode ion plating [5] reactive magnetron sputtering [3,6], vacuum arc deposition [7], pulsed arc technique [8], and plasma nitridition [9] have been reported.

Mild steel, which is an important structural material used for industrial applications, has been chosen as the metal substrate for evaluating the applicability of ZrN film in the present study. For a protective film material, corrosion resistance is one of most important properties in addition to its mechanical properties. Corrosion properties of a number of hard PVD nitride films have been recently reviewed by the authors[10]. Studies regarding the electrochemical [11] and thermal [12] oxidation of ZrN films are relatively scarce compared to those of TiN. More recently, ZrN has been used as a protective and decorative film, because of its superior corrosion resistance than the present commercial counterparts like TiN, CrN etc. Since ZrN has a higher negative free formation energy than TiN, ZrN seems to form itself more easily than TiN. For controlling the designed microstructures and physical properties of ZrN_X, thin films are technologically important [13]. The microstructure and properties of ZrN films will vary with different deposition techniques and processing parameters [14]. Substrate temperature (Ts) has a strong influence on the structural and morphological characteristics of the films, because it is correlated with thermal energy, employed to condense the material on the substrate surface [15]. A detailed experimental investigation is reported here on the structural, compositional, tribological and electrochemical corrosion properties of magnetron sputtered Zirconium Nitride films and on the effect of a Zirconium interlayer.

2. EXPERIMENTAL PROCEDURES

ZrN thin films of 1.5 microns thickness were deposited on mild steel substrate using a DC magnetron sputter deposition unit. The base vacuum of the chamber was below 1×10^{-4} Pa. High purity argon was fed into the vacuum chamber for plasma generation. The deposition parameters for ZrN reac-

*Corresponding author: bsmanian@cecri.res.in

Table 1. Optimized sputtering parameters for the deposition of ZrN thin film

Objects	Specification
Target	Zr (99.9%)
Substrates	Mild steel, Glass, Si (100)
Target to substrate distance	60 mm
Ultimate vacuum	1×10^{-6} m bar
Operating vacuum	2×10^{-3} m bar
Sputtering gas (Ar: N_2)	60:40
Power	180 Watt
Substrate temperature	200 °C

tive sputtering are summarized in Table 1.

The chemical nature of the outermost part of ZrN film was obtained by X-ray photoelectron spectroscopy (XPS) using Multilab 2000. A Renishaw Ramascope System 2000 spectrometer was used for Laser Raman experiments. The microscope attachment was an Olympus BH2 system. Power of 2–3 mW was incident on the samples in a 2 μm diameter spot through a standard ×50 microscope objective. The spectra with a 200 s data point acquisition time, spectral range of 100–1500 cm^{-1} and spectral resolution of 3–4 cm^{-1} were collected. Spectra were presented as intensity (counts) versus Raman shift (cm^{-1}). The thin films were characterized using a Shimadsu X-ray diffractometer with a CuKα radiation of wavelength 1.5414A°. Diffraction patterns were recorded with a step size of 0.01°, scan speed of 1s/step and scan angle 2θ from 10° to 130°. Crystallographic parameters were refined by Rietveld analysis using TOPAS-3. A ZrN structure was built by using Diamond software. The surface of the film was characterized by a molecular imaging Atomic Force Microscope.

Wear tests were carried out in a Block-on-Ring system. All tests were carried out at room temperature, ambient humidity and without lubrication. A steel ball bearing was used as a counter body. The ring material having a diameter of 60 mm was made of High Chromium High Carbon Tool Steel with Vickers hardness 850 HV. The load applied on-the specimen was 400 g (3.924 N) with the sliding speed of 100 rpm. The wear rate was calculated by measuring the weight change of a specimen before and after the test. The apparatus used for the Scanning Vibrating Electrode Technique (SVET) was Princeton Applied Research –SVP100. Important operating parameters were as follows: vibrating frequency, 81Hz; electrode amplitude, 30 μm pp; distance between center and coated steel surface, C_a 100 μm; scanning velocity, 500 μm/sec. A coated steel specimen was scanned repeatedly by a platinum vibrating electrode in the X-direction and with steps in the Y-direction between each scan where both X and Y coordinates were divided into 20 parts. The degree of E is proportional to the current density of corrosion.

Electrochemical polarization studies were carried out using an Autolab Electrochemical workstation. Experiments were conducted using a standard three-electrode configuration, with a platinum foil as the counter electrode, a saturated calomel electrode (SCE) as the reference electrode and the sample as the working electrode. The specimen (1.0 cm^2 exposed area) was immersed in the test solution of 3.5% NaCl. Experiments were carried out at room temperature (28 °C). In order to establish the open circuit potential (OCP), prior to measurements, the sample was immersed in the solution for about 60 min. Impedance measurements were conducted using a frequency response analyzer. The spectrum was recorded in the frequency range 10 mHz-100 kHz. The applied alternating potential had root mean square amplitude of 10 mV on the open circuit potential. After reaching the stable OCP, the upper and lower potential limits of linear sweep voltammetry were set at +/-200 mV with respect to OCP,, and the sweep rate was 1 mV s^{-1}. The Tafel plots were obtained after the electrochemical measurements.

3. RESULTS AND DISCUSSION

3.1. Compositional and structural analyses

Chemical states of the ZrN films were determined by X-ray photoelectron spectroscopy (XPS) and are shown in Fig. 1. A clearer result of the possible chemical bonding states of Zr with N for the film could be obtained from an individual XPS signal. The characteristic Zr 3d, N1s, O1s peaks were observed at the corresponding binding energies. The Zr 3d spectrum was fitted using a Gaussian peak shape to three components: a weak peak at 181 eV which was identified as $Zr3d_{5/2}$ originating from ZrN, a peak at 183 eV was from Zr (N,O) bonds and a peak at 185.35 eV which can be attributed to the presence of ZrO_2 in the film [16]. The associations between N1s peaks positions and compounds were: 396.8 eV to Zr_3N_4. 400.2 eV to ZrNx where x<1 [17]. The deficiency of nitrogen would cause nitrogen vacancies in the ZrN structure. This would lead to a peak shift on N1s core level spectra and to the formation of non-stoichiometric compounds (ZrNx with 0<x<1). The binding energy of these compounds lies between the binding energy lower limit of the absorbate species that were found at 400.2 eV in the as deposited samples. The experimentally revealed core shell shifts have been well explained in literature as the result of different N1s sites created by air exposure of the surface region [17].

The O1s signal presents two components associated with oxide and hydroxide species. The C1s peaks in the spectra (at 285.5 eV) may be from organic carbon, which is unavoidable when using an oil diffusion pump for evacuating the deposition chamber and XPS sample holding compartment [18].

In the EDS spectrum (Fig. 2), the major element present is identified as Zr and with less intensity N, corresponding to

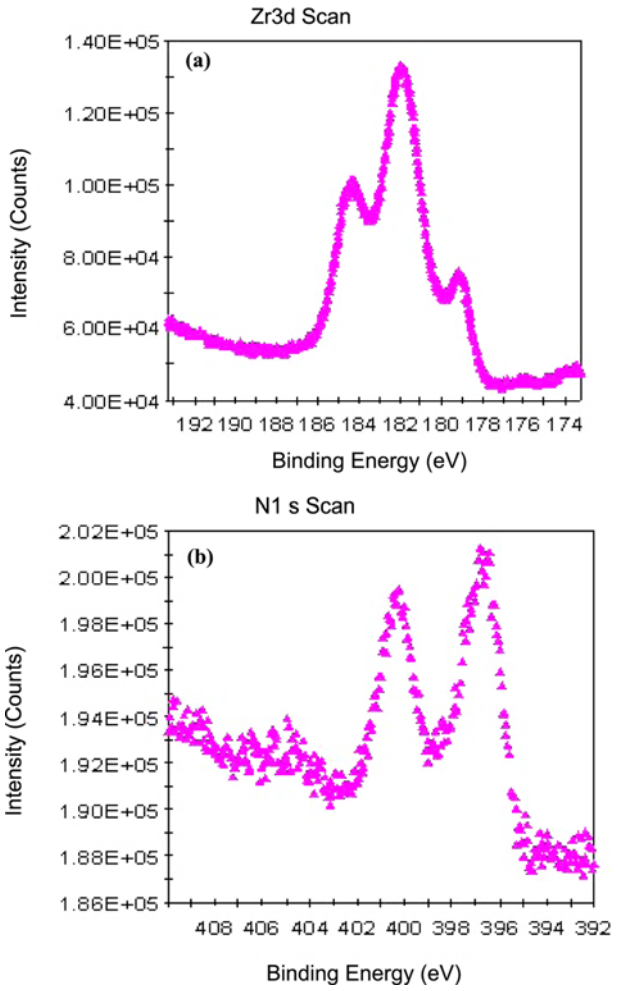

Fig. 1. X-ray Photo electron Spectroscopy spectra of (a) Zr 3d and (b) N1s.

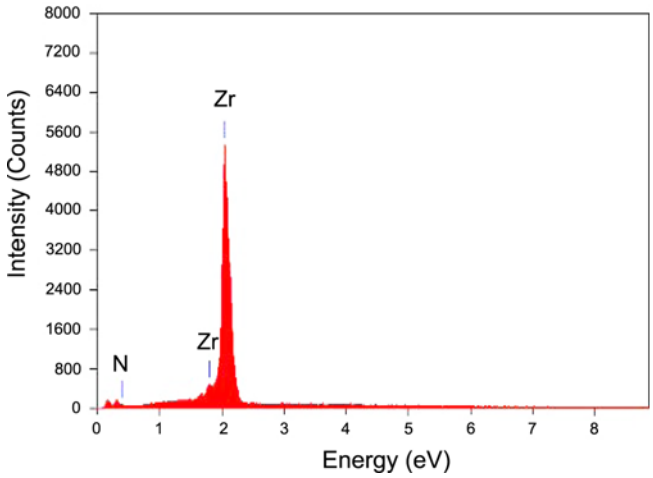

Fig. 2. EDS spectra of magnetron sputtered ZrN thin film.

the film, and other peaks that belong to the substrate. The films were characterized using Raman microscopy to elucidate the behavior of the optic and acoustic phonon modes of the face centered cubic crystalline lattices. The Raman spectra of ZrN films deposited at the optimized substrate temperature of 200 °C as shown in Fig. 3 consists of two broad bands centered at 222 cm^{-1} (FWHM=130 cm^{-1}) in the acoustic region, which is due to the vibrations of the heavy Zr ions, and in the optic region at 511 cm^{-1} (FWHM=230 cm^{-1}), which is due to the vibrations of the lighter N ions. This agrees with the Raman studies on ZrN films reported by Constable *et al*. [19].

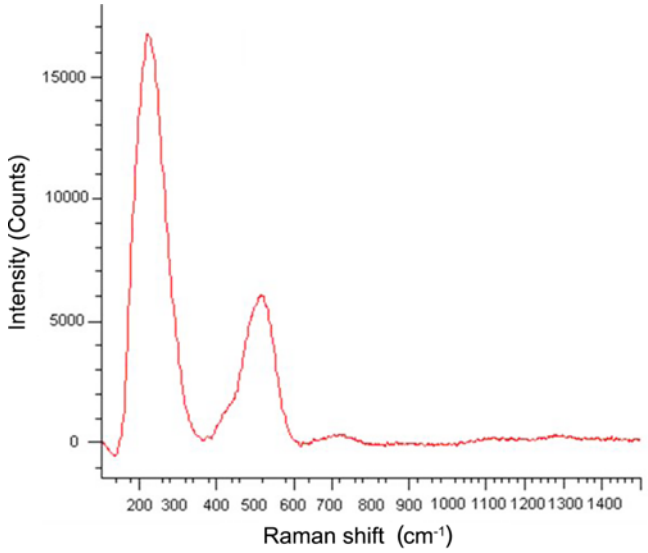

Fig. 3. Laser Raman spectra obtained for the sputtered ZrN thin film.

Rietveld refinement (Fig. 4) was carried out in order to examine the crystallographic parameters for cubic ZrN phase (space group of Fm-3m). The lattice parameters of "*a*"= 0.456 nm was calculated and the value was comparable with earlier reports [20]. The XRD peaks were matched to Si and SiO_2 cristobalite beta phases. Rietveld refinement were analyzed for the ZrN thin film; the mass percentages of ZrN (80.45%), Si (0.13%) and SiO_2 (4.94%) were calculated (Fig. 4). From the Rietveld refinement, the agreement factors were obtained for the ZrN thin films: the values of as expected refinement index, weighted refinement factor, profile refinement factor, Bragg refinement factor and goodness of fit are 10.40, 5.25, 1.24, 4.12 and 0.99, respectively. The bond length between nearest neighbors of Zr to N (x4) was calculated as 2.2875 Å (Fig. 4 -insert).

Ex-situ atomic force microscopy (AFM) has been used independently to assess the surface quality of the DC magnetron sputtered ZrN thin films. The AFM pictures of the thin films grown at 200 °C are shown in Fig. 5(a). The top view of the picture recorded in area of 5 μm×5 μm shows the presence of spherical granular structure on the top of the homogeneous granular surface. The irregular size of the grains suggests that at low substrate temperatures, the kinetic energy

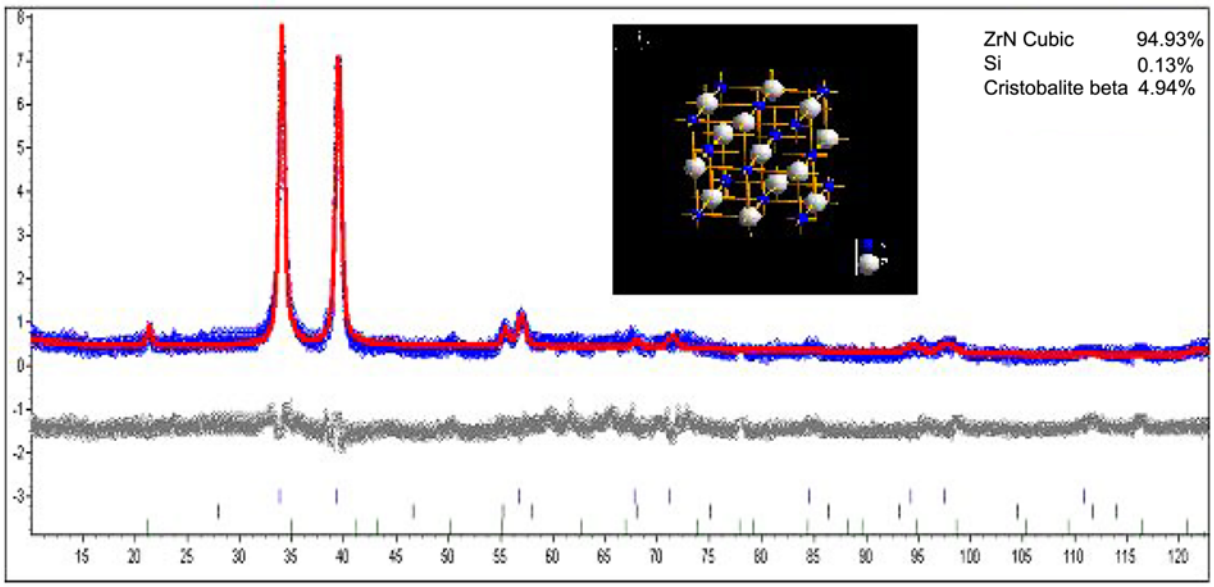

Fig. 4. Rietveld refinement of as prepared ZrN thin films deposited on Si by d.c. sputtering. (Insert) A unit cell of ZrN is constructed using the refined data by using Diamond software.

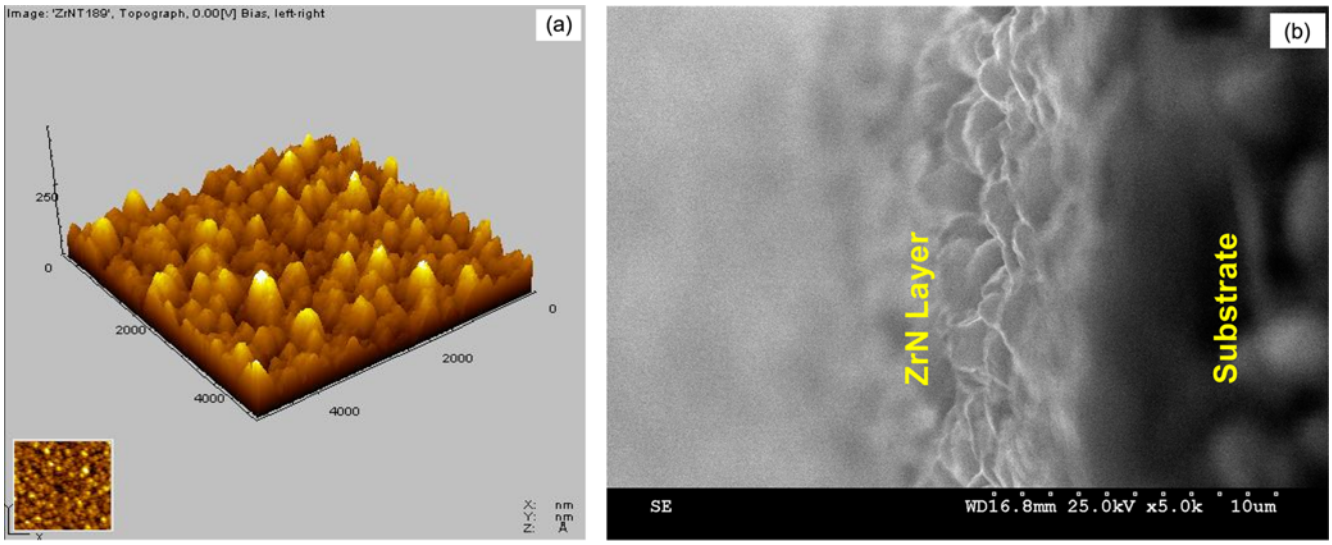

Fig. 5. (a) AFM picture of magnetron sputtered ZrN thin film and (b) Cross sectional SEM picture of magnetron sputtered ZrN thin film.

is not sufficient for the coalescence of the grains. The sputtered atomic or molecular species on the substrate surface acquire a large thermal energy and hence a larger mobility when deposited at higher substrate temperatures of about 400 °C. This enhances the diffusion distance of the sputtered species. As a result, the collision process initiates nucleation and enhances island formation in order to grow continuous film with larger grains. The cross section examination by SEM is shown in Fig. 5(b), which indicates the presence of columnar microstructures of the sputtered ZrN on mild steel substrate.

3.2. Tribological properties

The tribological characteristics of these films were measured using a block-on-ring test. The ring material used for this test was high chromium, high carbon, tool-steel (850 HV). Low and smooth friction behavior typified by a steady trace at an average friction coefficient value of 0.3 was observed for the ZrN/Zr/MS stack whereas a higher value of 0.5 was observed for the ZrN/MS specimen. The lower friction coefficient observed in Fig. 6 for the ZrN/Zr/MS stack indicated that the stack has better wear resistance. Sufficient coated layer and substrate hardness and superior adhesion of the

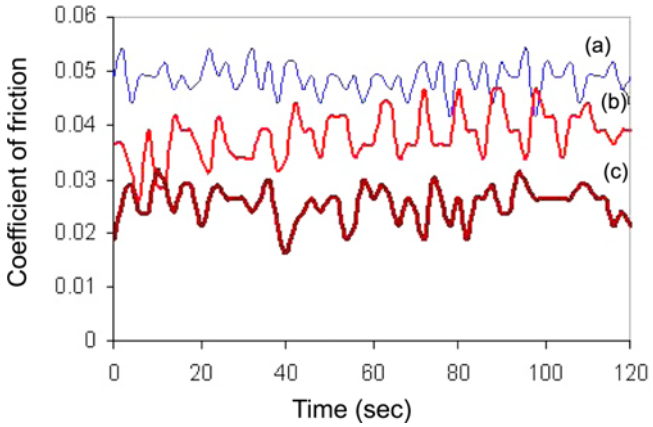

Fig. 6. The variation of co-efficient of friction with time for (a) MS, (b) ZrN/MS and (c) ZrN/Zr/MS.

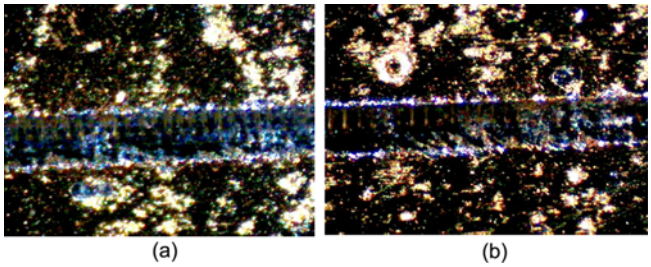

Fig. 7. Optical Micrographs of the worn surfaces of (a) ZrN/MS and (b) ZrN/Zr/MS film.

layer to the substrate are prerequisites for excellent wear properties of a coated material [21]. The wear tracks that formed on the surface of the coated samples are shown in Figs. 7(a) and (b). It is seen that the specimen is mainly abrasively worn out and plastic deformation of wear debris is clearly shown in the central region of Fig. 7(a) for the ZrN/MS sample.

Figure 8 displays a typical load-displacement curve from which the hardness can be evaluated using the following equation [22].

$$H=P_{Max}/A \quad (1)$$

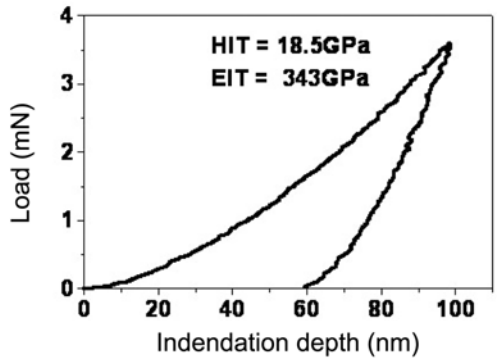

Fig. 8. Nanoindendation curve for ZrN thin film.

where P_{Max} is the maximum load, and A is the projected area determined from the function of depth. Upon unloading, the elastic displacements were recovered and the plastic displacements were retained. The indentation depth was lower than 100 nm, which in turn was lesser than 10% of the film thickness used. The nanohardness and Young's modulus of the ZrN films with a Zr interlayer prepared at 200 °C were 18.5 GPa and 343 GPa respectively. No appreciable change was observed for the ZrN film without an interlayer. The higher hardness value was observed because of the presence of strained domains.

3.3. Electrochemical corrosion studies

3.3.1. Scanning vibrating electrode and CV techniques

The scanning vibrating electrode technique (SVET) has been developed to allow high spatial resolution investigation of localized corrosion activity that may be associated with film defects or galvanic coupled regions of the metal surface. Using the SVET, minute variations in DC current or voltage associated with localized corrosion activity are detected and used to map both anodic and cathodic corrosion activities in a localized area. The difference in initial corrosion activity under various films can be correlated to the performance life of the films. In the current study, the SVET was used to discriminate the corrosion protection performance of selected coated systems. The potential gradients (E) caused by current flowing between the local anode and local cathode on coated steel samples were mapped and measured at 64 points within an area of 5000 μm^2.

The 2D and 3D maps of potential gradients (E) by SVET of MS, and ZrN/Zr/MS specimens in an aqueous solution of 3.5% NaCl after immersion for an hour are shown in Fig. 9. SVET was able to discretely map relative cathodic (blue in colour) and anodic sites (red in colour) at a macroscopic defect and to record the changes of local electrode activities in real time. The E is developed around the corroded metal surface due to the ionic current between the local anodic and cathodic areas. The distribution of E leads to an evaluation of the corrosion behavior of the metal interims of current density. By summing the anodic and cathodic potentials measured using SVET for each scan, a quantitative comparison was made and shown in Fig. 9. The E increased in the following order ZrN/Zr/MS < ZrN/MS < MS. The results exhibit good corrosion resistance of a ZrN film with a Zr interlayer.

3.3.2. Tafel polarization

The E_{corr} and I_{corr} values have been calculated using the Tafel extrapolation method (Fig. 10). There is an appreciable increase in corrosion resistance of the ZrN with a Zr interlayer on MS compared to ZrN on MS and bare MS substrate. The corrosion resistance of the specimens was estimated from anodic polarization curves in a 3.5% NaCl solution. Each polarization curve represents the mean of the values

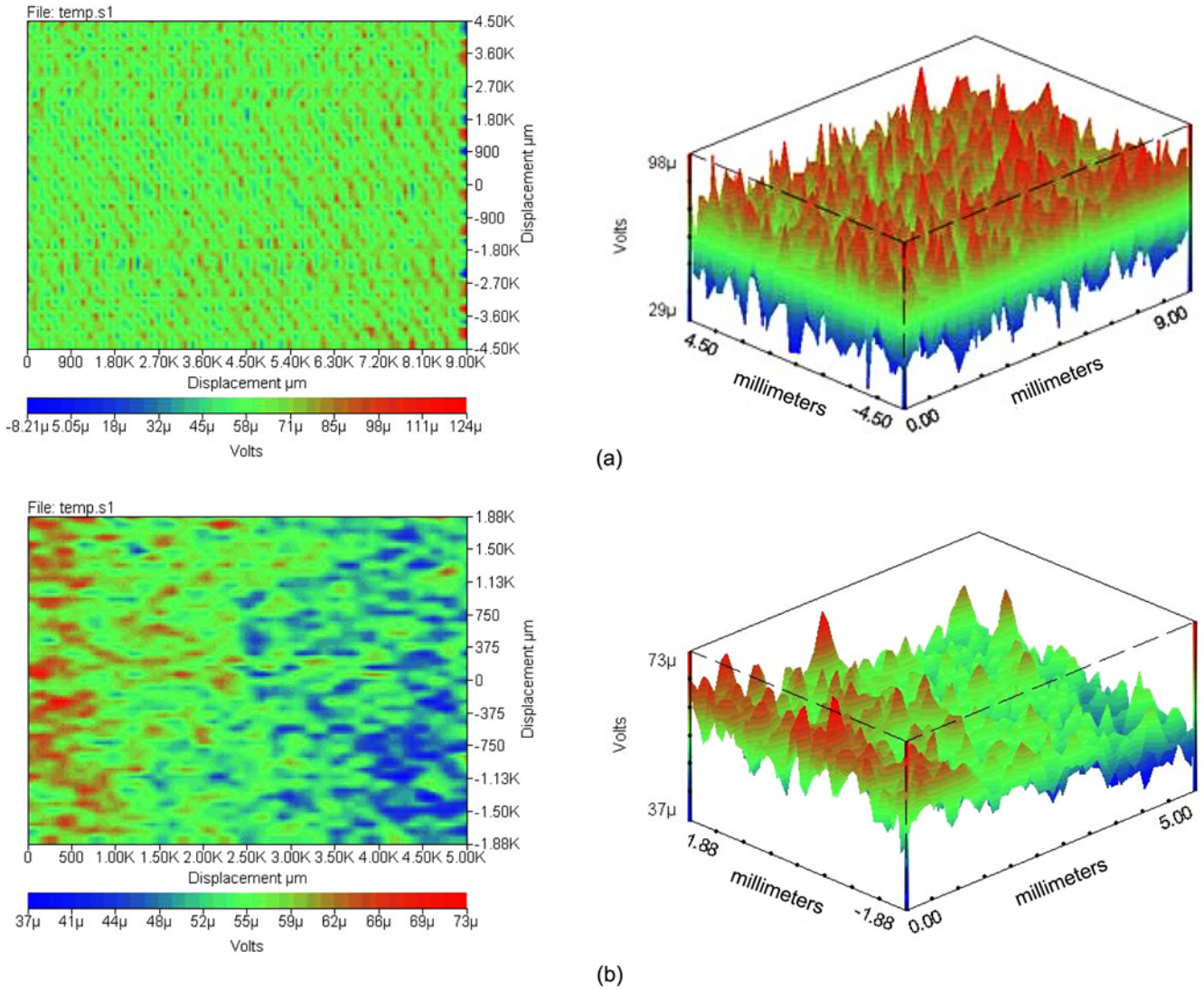

Fig. 9. SVET pictures obtained for the (a) MS, (b) ZrN/Zr/MS.

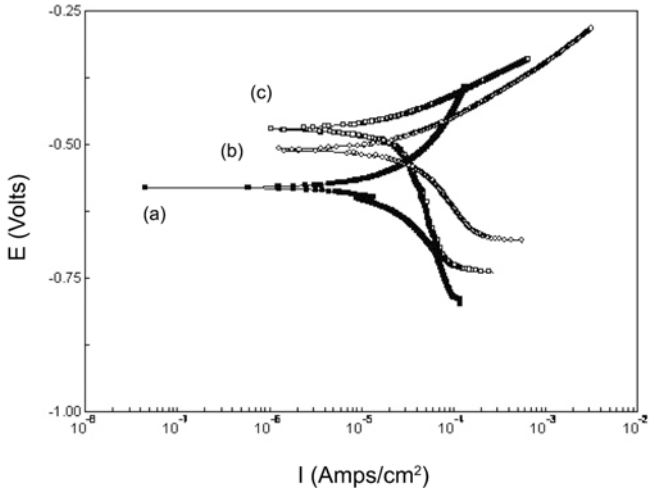

Fig. 10. The potentio dynamic polarization curves in 3.5%NaCl solution for (a) MS substrate, (b) ZrN/MS and (c) ZrN/Zr/MS.

obtained for these films. The corrosion potential (E_{corr}) and current densities (I_{corr}) are determined from their polarization curves using the Tafel slopes β, α and β, c. and polarization resistance (R_p). The corrosion rate is normally proportional to the corrosion current density (I_{corr}), which is calculated based on the cathodic part of the polarization curve.

ZrN film on MS samples improved the corrosion resistance by decreasing the corrosion current and increasing the corrosion potential. Although the ZrN layer provides a corrosion barrier, there could be high interfacial stress between the film and substrate, in turn leading to film spilling when the sample is immersed in the NaCl solution for electrochemical testing. Due to the presence of small pinholes in the films, rapid localized corrosion of MS substrate takes place at these defects and even leads to debonding of the films. This may also be due to the combined effect of the

Table 2. Polarization and impedance data of ZrN film and with a Zr interlayer on mild steel substrates in a 3.5%NaCl solution

Sample	E_{corr} Vs SCE	b_a	b_c	I_{corr}	R_{ct}	C_{dl}
	/V	/V dec^{-1}	/V dec^{-1}	/A cm^{-2} × 10^{-5}	/Ω cm^2	/F cm^{-2}×10^{-6}
MS	–0.594	0.15	–0.14	6.3	332.1	167
ZrN/MS	–0.510	0.09	–0.21	3.5	524.6	151
ZrN/Zr/MS	–0.457	0.07	–0.51	1.4	1605.9	2.8

rather noble steady state potential of the ZrN film and relatively active iron species. The potentiodynamic curves for ZrN films with pinholes, therefore, mimic the behavior of mild steel substrate.

The results of corrosion testing for the substrate and sputtered ZrN with a Zr interlayer, ZrN on MS and for the steel substrate are shown in Table 2. The corrosion current of the MS substrate is greater than that of sputtered ZrN. The presence of 2 μm thick Zr interlayer before the ZrN film clearly reduces the corrosion current. The surface ZrN/Zr layer significantly decreases the corrosion rate of the MS substrate.

3.3.3. AC impedance studies

The same three-electrode cell stack, as used for the potentiodynamic polarization experiments, was employed for the AC impedance investigations. Impedance measurements were made at open circuit potential (OCP) by applying an AC signal of 10 mV in the frequency range of 10 mHz to 100 kHz. The Nyquist plots for the samples used for corrosion tests in 3.5% w/v NaCl solution are shown in Fig. 11. The double layer capacitance C_{dl} value is obtained from the frequency at which Z imaginary is maximum [23].

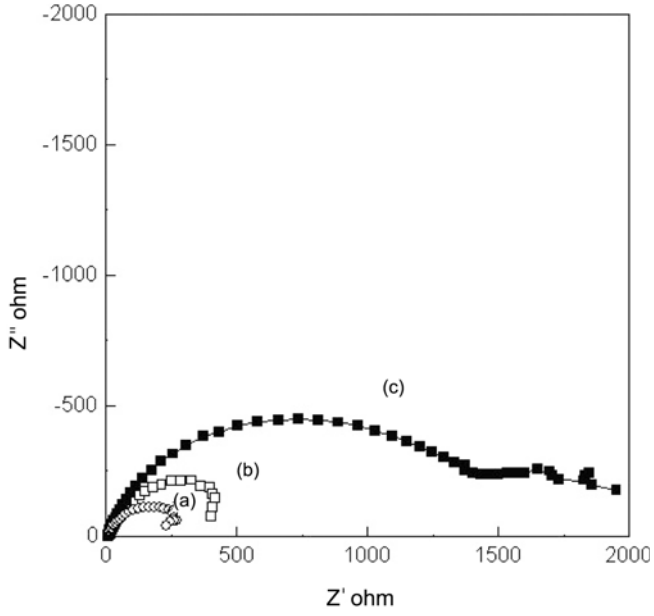

Fig. 11. Nyquist plots of (a) MS substrate, (b) ZrN/MS and (c) ZrN/Zr/MS.

$$\omega\,(Z_{(im)}\max) = 1/C_{dl}\,R_{ct.} \quad (2)$$

At higher frequencies the interception of real axis in the Nyquist plot is ascribed to the solution resistance (R_s) and at the lower frequencies, the interception with the real axis is ascribed to charge transfer resistance (R_{ct}). When the sample is immersed in the electrolyte, the defects in the film provide a direct diffusion path for the corrosive media. In this process, the galvanic corrosion cells are formed and localized corrosion dominates the corrosion process. A higher Rct value was observed (Table 2) for the ZrN /Zr/ MS substrate than the ZrN film on MS and the bare MS substrate shows that ZrN on steel substrate with Zr interlayer has higher corrosion resistance.

4. CONCLUSIONS

Zirconium Nitride films were deposited by reactive DC magnetron sputtering on mild steel substrates. The film demonstrated polycrystalline nature with FCC structures, observed from the XRD. The adhesion of ZrN/Zr/MS stack layer was found to be much better and peeled off only at a higher critical load of 98 N than that the ZrN films without an interlayer. Low and smooth friction behavior with a friction coefficient of 0.3 was observed for ZrN/Zr/MS stack whereas a higher value of 0.5 was observed for the ZrN/MS specimen which again proved that the Zr interlayer provides a good load support for the film and hence wear resistance. The nanohardness of the ZrN films with a Zr interlayer was found to be 18.5 GPa. It can be seen from the polarization curves that ZrN with a Zr interlayer specimen had a significantly higher corrosion potential (–0.457V) and found to be nobler than that for samples (–0.510V for ZrN and –0.594 V for the bare substrate). Also a higher value of charge transfer resistance of 1605.9 Ω cm^2 was noticed for the film with an interlayer which indicated that the ZrN/Zr/MS stack had a weaker tendency towards corrosion in 3.5% w/v NaCl.

ACKNOWLEDGMENTS

One of the authors (B.S.) thanks the Department of Atomic Energy (DAE), Board of Research in Nuclear Sciences (BRNS), Mumbai, for a research grant (Sanction No 2006/37/37/BRNS/2068) and Japan Society for the Promotion of

Science, Japan for the award of FY 2011 JSPS Long term Invitation fellowship.

REFERENCES

1. W. J. Chou, C. H. Sun, and G. P. Yu, *Mater. Chem. Phys*. **82**, 228 (2003).
2. A. Mitsuo, T. Mori, and Y. Setswhar, *Nucl, Instrum. Methods* **206**, 366 (2003).
3. A. Rizzo, M.A. Signore, L. Mirenghi, and D. Dimaio, *Thin Solid Films* **515**, 1486 (2006).
4. R. Sanjines's, C.S. Sandu, R. Lamni, and F. Hevy, *Surf. Coat. Tech.* **200**, 6308 (2006).
5. C. H. Ma, J. H. Huang, and H. Chen, *Surf. Coat. Technol*. **133-134**, 289 (2000).
6. C.-P. Liu and H.-G. Yang, *Thin Solid Films* **444**, 111 (2003).
7. V. N. Zhitomirsky, I. Grimberg, R. L. Boxman, N. A. Travitzky, S. Goldsmith, and B. Z. Weiss, *Surf. Coat. Technol*. **94-95**, 207 (1997).
8. H. Jimenez, E. Restrepo, and A. Devia, *Surf. Coat. Technol.* **201**, 1594 (2006).
9. L. Pichon, A. Straboni, T. Girardean, and M. Drouet, *J. Appl. Phys*. **87**, 925 (2000).
10. I. Milosev, B. Navinsek, and H-H. Strehblow, *Scientific Series of the International Burean,* Forschungszentrum Jilich Gmbh. **37**, 146 (1995).
11. R. Brown, M. N. Alias, and R. Fontana, *Surf. Coat. Technol.* **53**, 25 (1992).
12. I. Milosev, H.-H. Strehblow, and B. Navinsek, *Thin Solid Films* **203**, 246 (1991).
13. J.-H. Huang, C.-Y. Hsu, S.-S. Chen, and G.-P. Yu, *Mater. Chem. Phys.* **77**, 14 (2003).
14. D.-J. Kim, Y.-M. Yu, S.-H. Eorn, T.-H. Kim, C.-S. Go, and Y. D. Choi, *Mater. Chem. Phys.* **92**, 274 (2005).
15. H. M. Beria, M. Guemmaz, G. Schmerber, A. Mosser, and J. C. Perlebas, *Appl. Surf. Sc.* **211**, 146 (2003).
16. D. Wu, Z. Zhang, W. Fu, X. Fan, and H. Guo, *Appl. Phys. A* **64**, 593 (1997).
17. A. Rizzo, M. A. Signore, L. Mirenghi, and D. Dimaio, *Thin Solid Films* **515**, 1486 (2006).
18. B. Subramanian, C. V. Muraleedharan, R. Ananthakumar, and M. Jayachandran, *Surf. Coat. Technol.* **205**, 5014 (2011).
19. C. P. Constable, J. Yarwood, and W. D. Munz, *Surf. Coat. Tech.* **116-119**, 155 (1999).
20. J.-H. Huang, C.-H. Ho, and G.-P. Yu, *Mater. Chem. Phys.* **102**, 31 (2007).
21. K. H. Ko, J. H. Ahn, C. S. Bae, and H. S. Chung, *Korean J. Mater. Res.* **5**, 960 (1995).
22. W. C. Oliver and G. M. Phar, *J. Mater. Res.* **7**, 1564 (1992).
23. B. Subramanian, R. Ananthakumar, and M. Jayachandran, *Surf. Coat. Technol.* **205**, 3485 (2011).